

DALNet: A Rail Detection Network Based on Dynamic Anchor Line

Zichen Yu, Quanli Liu, *Member, IEEE*, Wei Wang, *Senior Member, IEEE*,
Liyong Zhang, *Member, IEEE*, and Xiaoguang Zhao

Abstract—Rail detection is one of the key factors for intelligent train. In the paper, motivated by the anchor line-based lane detection methods, we propose a rail detection network called DALNet based on dynamic anchor line. Aiming to solve the problem that the predefined anchor line is image agnostic, we design a novel dynamic anchor line mechanism. It utilizes a dynamic anchor line generator to dynamically generate an appropriate anchor line for each rail instance based on the position and shape of the rails in the input image. These dynamically generated anchor lines can be considered as better position references to accurately localize the rails than the predefined anchor lines. In addition, we present a challenging urban rail detection dataset DL-Rail with high-quality annotations and scenario diversity. DL-Rail contains 7000 pairs of images and annotations along with scene tags, and it is expected to encourage the development of rail detection. We extensively compare DALNet with many competitive lane methods. The results show that our DALNet achieves state-of-the-art performance on our DL-Rail rail detection dataset and the popular Tusimple and LLAMAS lane detection benchmarks. The code will be released at <https://github.com/Yzichen/mmlaneDet>.

Index Terms—Rail detection, lane detection, intelligent train, dynamic anchor line mechanism

I. INTRODUCTION

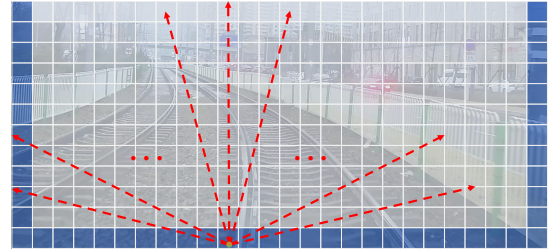
INTELLIGENT train uses advanced sensors and algorithms to assist or replace the driver in perceiving and analysing the train’s operating environment, which can reduce the risk of accidents caused by human drivers, and has gradually become a mainstream trend in the development of rail transit. As an important safety guarantee for train operation, active obstacle detection has become one of the necessary functions of intelligent train [1], [2]. In particular, the accurate rail detection can provide the travelling limits of the train as an important prerequisite for active obstacle detection, so it should be regarded as an important research area like lane detection.

Despite the importance of the rail detection task, its development is relatively slow. One important reason is that there is still a lack of public challenging rail detection datasets.

(Corresponding author: *Quanli Liu*).

Zichen Yu, Quanli Liu, Wei Wang and Liyong Zhang are with the School of Control Science and Engineering, Dalian University of Technology, Dalian 116024, China, and also with the Dalian Rail Transmit Intelligent Control and Intelligent Operation Technology Innovation Center, Dalian 116024, China (e-mail: yuzichen@mail.dlut.edu.cn; liuql@dlut.edu.cn; wangwei@dlut.edu.cn; zhly@dlut.edu.cn).

Xiaoguang Zhao is with the Dalian Rail Transmit Intelligent Control and Intelligent Operation Technology Innovation Center, Dalian 116024, China, and also with the Dalian Seasky Automation Co., Ltd, Dalian 116024, China (e-mail: xiaoguang.zhao@dlssa.com).



(a) predefined anchor lines



(b) dynamic anchor lines

Fig. 1. Illustration of different anchor lines. (a) The predefined anchor lines are generated by placing fixed anchor lines with different slopes at each image boundary point. The blue grid cells represent the image boundary regions and the red dashed arrows represent the corresponding anchor lines. (b) The dynamic anchor lines are generated based on the position and shape of the rails in the input image, they correspond to the rails one by one and fit more closely to the rails.

Therefore, we firstly mount cameras on a 202-line tram in Dalian, Liaoning Province, China, to collect data, and create the rail detection dataset DL-Rail, which consists of 7000 pairs of images and annotations along with scene tags. Most of the images in the existing rail detection datasets [3], [4] are collected in intercity railway scenarios, which are relatively homogeneous. Compared with them, our dataset is collected under urban railway scenarios, which contains richer and more complex railway scenarios under different rights-of-way, diverse weather, and varying lighting conditions. For example, in public right-of-way scenarios, the oncoming vehicles and pedestrians may cause occlusion of the rails, which is a situation that is missing in existing datasets.

With this dataset in hand, we turn our attention to how to design a good rail detection algorithm. Previous rail detection methods can be roughly classified into traditional hand-crafted rail detection methods and deep learning-based rail detection methods. Among them, traditional hand-crafted rail detection methods [5]–[8] usually use edge features and straight-line features of the rail for detection, but they are not robust

enough to cope with real-world environments. Deep learning based rail detection methods [3], [4], [9] use Convolutional Neural Networks (CNNs) to extract features and are more advantageous in terms of accuracy and robustness. More importantly, many well-developed deep learning based lane detection methods [10]–[13] can also provide many valuable references for their design, since lanes are similar to rails in that they all have slender shapes.

The lane detection methods can be classified into segmentation-based methods [14]–[18], anchor-based methods [11], [12], [19]–[21], keypoint-based methods [13], [22]–[24], and curve parameter-based methods [25]–[29]. In particular, anchor-based methods are well suited for rail detection due to their effectiveness and high efficiency. Specifically, LaneATT [11] places a large number of anchor lines (*e.g.*, 2782) at the image boundaries as references as illustrated in Fig. 1(a), and then uses feature pooling to obtain features of the region of interest (RoI) corresponding to the anchor lines, which are used to predict the offsets between the lanes and the anchor lines. When applied to rail detection, these predefined anchor lines are able to naturally distinguish between different rail instances and also mitigate the occlusion problem by predicting the rail as a whole unit. However, this also introduces several problems. Firstly, the number of anchor lines is excessive for rails, and only very few anchor lines are actually active during inference, which results in a waste of computational and memory resources. And simply reducing the number of anchor lines will cause them to fail to cover the potential locations of the rails. Secondly, these anchor lines are image-agnostic and may have a large deviation from the rails, posing difficulties in the localization and identification of the rail. In addition, these anchor lines lead to many duplicate predictions that require the non-maximum suppression (NMS) post-processing to eliminate, introducing additional time-consumption and complexity.

To overcome the above limitations, in this paper, we design a dynamic anchor line mechanism, based on which a novel rail detection model called DALNet is proposed. As shown in the Fig. 1(b), it dynamically generates an appropriate anchor line for each rail instance according to the position and shape of the rail in the input image instead of predefined lines. Specifically, we propose a dynamic anchor line generator consisting of three parallel lightweight prediction branches that predict the starting point heatmap, the starting point compensation offset and the slope (which represents the angle between the anchor line and the image x-axis) of the anchor line, respectively. The corresponding anchor line for each rail instance can then be constructed from the predicted starting point coordinate and slope. In the training phase, we utilize the starting point of the rail to generate the starting point label of the anchor line, and compute the average angle between the sampled points on the rail and the starting point as the ground truth value of the slope, so that the dynamically generated anchor line is more fitting to the rail, and can be used as a better reference. In addition, in the inference phase, in order to construct the anchor line, we use a simple max pooling and AND operation to find the peaks in the starting point heatmap, which can eliminate duplicate predictions and is more efficient than NMS.

To summarise, our main contributions are summarized as follows::

- We propose a novel dynamic anchor line-based rail detection model called DALNet, where a dynamic anchor line generator generates an appropriate anchor line for each rail instance based on the input image, which not only provide a better reference for rail detection, but also eliminates the need for time-consuming NMS post-processing.
- We present an urban rail detection dataset DL-Rail with high-quality annotations and scenario diversity, expected to facilitate the development of rail detection.
- Without bells and whistles, our proposed DALNet achieves state-of-the-art performance on our DL-Rail dataset. Moreover, it has high accuracy while ensuring high efficiency, *e.g.*, a 96.43 F1@50 score and 212 FPS on DL-Rail.
- Inspiringly, DALNet also shows superior performance on the popular lane detection benchmarks Tusimple [30] and LLAMAS [31], which further proves the effectiveness of our DALNet and also shows that the dynamic anchor line mechanism also has application potential in the field of lane detection.

II. RELATED WORKS

A. Rail Detection Methods

According to the manner of feature extraction, rail detection methods can be categorized into image processing-based methods and deep learning-based methods.

1) *Image processing-based methods*: Image processing-based methods usually utilize hand-crafted geometric features of the rails to detect the rails. Nassu *et al.* [5] extract the rails by matching the edge features with the rail patterns modeled as a sequence of parabolic segments, where the rail patterns in the near and far regions are precomputed offline and generated on-the-fly, respectively. Qi *et al.* [6] extract the histogram of oriented gradients (HOG) features and generate an integral image, and then detect the rails based on a region growing algorithm. Zwemer *et al.* [7] propose a generalized tram rail detection system that combines the inverse perspective transform and a priori geometric knowledge of the rail to find rail segments, and also establishes a rail reconstruction algorithm based on graph theory. Zheng *et al.* [8] segment the input image equally along the vertical axis, then approximate the edges as multiple line segments, and finally, fit the rail curve using the least squares method after filtering the terminals of the line segments. These methods are fast enough and do not require a high-performance computing platform, but their performance is vulnerable to environmental changes.

2) *Deep learning-based methods*: Deep learning-based rail detection methods generally rely on CNN for feature extraction. Wang *et al.* [3] convert rail detection into a single-category semantic segmentation task and utilize the top-down pyramid structure to extract features, showing good results on their self-built dataset RSDS. Wang *et al.* [9] also adopt the semantic segmentation scheme and propose a multi-scale prediction network to predict the rail area and the forward

train area, which makes better use of global information and local characteristics by adequately fusing high-resolution and low-resolution feature maps. Motivated by the lane detection method UFLD [10], Li *et al.* [4] propose an efficient row-based rail detection method, which first samples the row anchors uniformly along the vertical direction of the image, and then localizes the rails by predicting the categorical position distributions corresponding to each row anchor. While these deep learning-based methods are more robust and accurate than image processing-based methods, they are relatively slow to develop and rely more on segmentation methods with unsatisfactory performance.

B. Lane Detection Methods

According to the representation of the lane, existing CNN-based lane detection can be divided into four categories: segmentation-based methods, anchor-based methods, curve parameter-based methods, and keypoint-based methods.

1) *Segmentation-based methods*: The segmentation-based lane detection methods adopt a pixel-level prediction formulation to treat lane detection as a semantic segmentation or instance segmentation problem. Since conventional CNNs are ineffective in detecting objects with slender structures or being occluded, SCNN [14] proposes a slice-by-slice CNN structure to pass messages between adjacent rows or columns in the feature maps, which can extract richer spatial information but is very time-consuming. RESA [15] enables horizontal or vertical information aggregation in a parallel manner by recurrently shifting sliced feature maps. It not only reduces the time cost, but also prevents information loss during propagation. Fast-HBNet [16] uses the composite transform and the proposed hybrid branching network to generate four feature maps with different receptive fields and spatial contexts, allowing the model to capture lane features of different shapes, scales, and views. These above methods assign a unique semantic category to different lane lines and require a predefined number of lanes. To cope with the problem of lane changes, Lanedet [17] treats lane detection as an instance segmentation problem, which disentangles the binary segmentation results into different lane instances using the predicted lane embeddings. [18] additionally introduces a lane center prediction branch and proposes a center-based lane discrimination method instead of the commonly used time-consuming Mean-shift clustering [32], which improves the efficiency and robustness.

2) *Anchor-based methods*: Anchor-based lane detection methods can be divided into row anchor-based methods and line anchor-based methods.

The row anchor-based methods formulate lane detection as a classification problem on predefined row anchors uniformly distributed over the image. UFLD [10] is a pioneering work using this scheme, which uses global features to directly predict lane position at each row anchor and achieves ultra-fast inference. Based on this, UFLDV2 [19] proposes a hybrid anchors scheme to alleviate the magnified localization error problem. CondLaneNet [12] proposes a conditional lane detection strategy based on conditional convolution and row

anchor formulation, which solves the lane instance level discrimination problem with lane starting points detection.

For the line anchor-based methods, they lay many anchor lines on the image as references and accurately localize the lanes by regressing the offsets. Inspired by the anchor box in object detection field, Line-CNN [20] is the first to propose to use the rays with different angles emitted from the image boundaries as the anchor lines, and then to predict the offset between the anchor line and the lane at each sliding window position over three boundaries. Following the same anchor lines setting, LaneATT [11] further introduces anchor-based feature aggregation and attention mechanisms to explore the local and global information of the lane, respectively, resulting in a better accuracy-speed tradeoff. CLRNet [21] uses learnable sparse anchor lines which will be optimized as network parameters during training. The optimized anchor lines represent the potential locations of lanes in the dataset. In conjunction with a cross-level lane refinement scheme, it achieves superior lane detection results. However, both predefined and learnable anchor lines are fixed and image-agnostic. In this paper, we propose a novel dynamic anchor line mechanism to dynamic generate an appropriate anchor line for each rail instance as a better reference.

3) *Curve parameter-based methods*: The curve parameter-based lane detection methods fit the lane by predicting the curve parameters. PolyLaneNet [25], LSTR [26], and PRNet [27] model the lane as a polynomial curve (e.g., $x = ay^3 + by^2 + cy + d$), and the polynomial coefficients corresponding to each lane instance are predicted. However, the learning of the abstract polynomial coefficients is not trivial, causing their performance to lag behind other methods. BézierLaneNet [28] and BSNNet [29] respectively utilize the parametric Bézier curve and B-spline curve to represent a lane. They transform lane detection into a control points prediction task and a achieve results competitive with other kinds of methods.

4) *Keypoint-based methods*: The keypoint-based lane detection methods transform the lane detection task into a keypoint detection and association problem. PINet [22] predicts keypoints and feature embeddings by stacked hourglass modules [33], and clusters keypoints based on the similarity of feature embeddings during post-processing. FoLoLane [23] constructs the local geometry by predicting the offset from each pixel to its three neighboring keypoints, which naturally enables the local association between keypoints. GANet [13] and DevNet [24] propose a more efficient global association strategy that finds the corresponding lane instance by predicting the offset from each keypoint to the lane starting point.

III. METHOD

The essence of our DALNet framework is to dynamically generate an appropriate anchor line as reference for each rail instance based on the position and shape of the rails in the image, instead of fixed and image-agnostic anchor lines. The overall architecture is shown in Fig. 2.

The DALNet is a simple and efficient network consisting of a feature extractor, a dynamic anchor line generator and

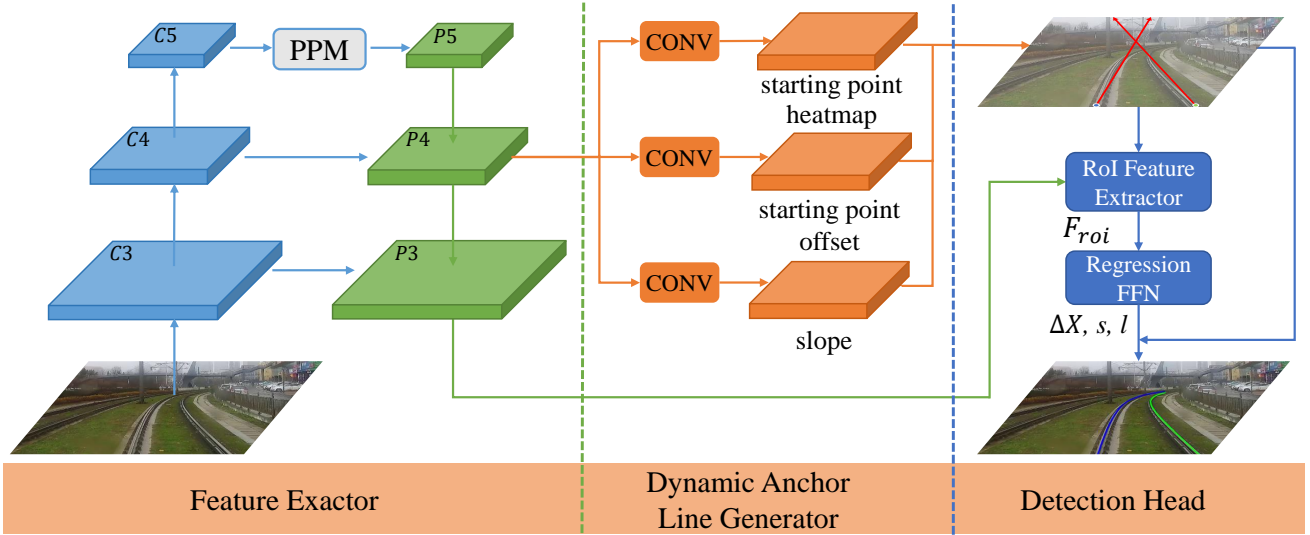


Fig. 2. Framework of DALNet. DALNet consists of three main components: feature extractor, dynamic anchor line generator and rail detection head. Given an input image, the feature extractor extracts multi-scale features and the pyramid pooling module (PPM) is employed to enlarge the receptive field. The dynamic anchor line generator includes three parallel branches that predict the starting point, offset and slope of the anchor line. Based on these predictions, the generator constructs a fitting anchor line for each rail instance. In the detection head, the generated anchor line is taken as a reference to localize the rail by predicting the horizontal offset between the rail and the anchor line.

a rail detection head. Given a forward-looking image $I \in \mathbb{R}^{3 \times H_I \times W_I}$ taken by a camera mounted in front of the train, this image is fed to the feature extractor to generate multi-scale rich features, where a pyramid pooling module (PPM) [34] is used to enlarge the receptive field and gather global context information. In the dynamic anchor line generator, the image features are fed into three parallel branches to predict the starting point, offset, and the slope of the anchor line, then an anchor line is dynamic constructed for each rail instance based on these predicted results. This generated anchor line is used as a reference in the rail detection head to accurately localize the rail by predicting the horizontal offset.

A. Rail and Anchor Representation

Rails are similar to lanes in that they both have a slender appearance structure. Therefore, we follow the lane representation in [11], [20] by representing a rail as a sequence of N_{pts} points, *i.e.*, $P = \{(x_0, y_0), (x_1, y_1), \dots, (x_{N_{pts}-1}, y_{N_{pts}-1})\}$, where the y coordinates of these points are fixed and uniformly sampled along the vertical axis of the image, *i.e.*, $y_i = \frac{H_I}{N_{pts}-1} \times i$. In addition, the start index s and the length l are used to describe the range of the rail in the vertical axis.

Different from common object detection [35], [36], we utilize anchor lines instead of anchor boxes to provide the position priors for rails, since rails are usually global and slender. The anchor line can be regarded as a ray emitted from the image boundary with a certain slope, so it can be parameterized as $(x_{start}, y_{start}, \theta)$, where (x_{start}, y_{start}) denotes the starting point coordinate and θ denotes the slope. However, existing methods usually use predefined or learnable anchor line parameters, which are independent of the current input image. In this paper, we use a new dynamic anchor line mechanism. It determines the anchor line parameters according to the position and shape of the rails in the input image

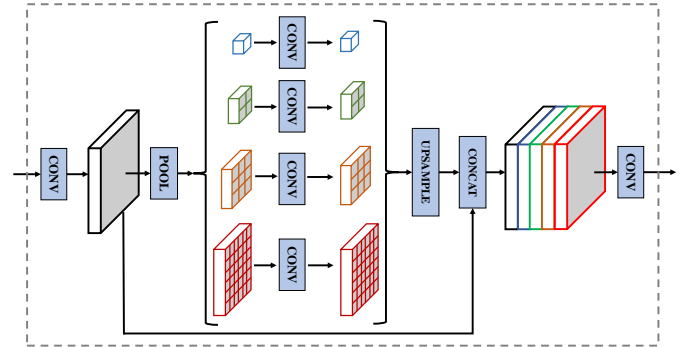


Fig. 3. The structure of the PPM. PPM performs pooling operations with different scales on the input feature map to establish a pooled feature pyramid. By fusing features at different pyramid scales through concatenation operation, PPM effectively enlarge the receptive field and gathers global context information.

and dynamically constructs a fitting anchor line for each rail instance.

B. Feature Extractor

Since both high-level semantic features and low-level geometric features are important for the rail detection, a feature pyramid network (FPN) [37] based on the standard ResNet architecture (*e.g.*, ResNet18) is employed to combine the multi-level features of the input image by constructing a feature pyramid with levels $P3$ to $P5$. To ensure efficiency, all pyramid feature maps have $C = 64$ channels.

In addition, the generation of dynamic anchor line requires the perception of the overall characteristics of the rail, so the ability to establish long-distance dependencies is necessary. To this end, we introduce the PPM [34] which has been shown to be effective in semantic segmentation, and insert it between the

ResNet backbone and the FPN neck. As shown in Fig. 3, The PPM pools the input feature map to different sizes, creating a pyramid of pooled features, with each layer of the pyramid having a different receptive field. By upsampling the pooled features and then concatenating them together for fusion, it can effectively enlarge the receptive field and capture global information at different scales. In the current work, we set up four fixed-size average pooling modules for PPM: 1×1 , 2×2 , 3×3 and 6×6 .

C. Dynamic Anchor Line Generator

The purpose of the dynamic anchor line generator is to generate a fitting anchor line for each rail instance based on the extracted image features. The anchor line can be determined based on its starting point and slope, thus in this paper, we decompose the generation of the anchor line into the starting point estimation and the slope estimation tasks.

1) *Starting Point Heatmap Estimation*: To estimate the starting point location, we design a keypoint detection branch consisting of two convolutional layers. It takes the $P4$ feature map as input and outputs a heatmap $\hat{P} \in \mathbb{R}^{H_4 \times W_4}$ to represent the probability that each pixel belongs to the starting point.

In the training stage, we simply use the starting point of the rail to generate the ground-truth heatmap. Specifically, Given a set of starting points of the rails $p_k = (x_k, y_k)$, $k = 1, \dots, N$, their downsampled positions $\tilde{p}_k = (\tilde{x}_k, \tilde{y}_k) = (\lfloor x_k/\delta \rfloor, \lfloor y_k/\delta \rfloor)$ in the feature map are computed, where $\delta = 16$ is the stride of the feature map. Then the ground-truth heatmap P is calculated as a smooth gaussian region of width σ around the starting point. The label at position (i, j) of the resulting heatmap P is given by:

$$P(i, j) = \max_k \exp\left(-\frac{(i - \tilde{x}_k)^2 + (j - \tilde{y}_k)^2}{2\sigma^2}\right), \quad (1)$$

where $(i, j) \in [0, W_4] \times [0, H_4]$ is the spatial indices of the heatmap and the standard deviation σ is related to the size of the input image.

The penalty-reduced focal loss [38] is applied to the predicted heatmap to resolve the imbalance between the starting point region and the non-starting point region. Let \hat{P}_{ij} and P_{ij} be the predicted and ground-truth label at the location (i, j) in the heatmap respectively, the starting point estimation loss is defined as:

$$\mathcal{L}_{heat} = -\frac{1}{N_p} \sum_{j=1}^{H_4} \sum_{i=1}^{W_4} \begin{cases} (1 - \hat{P}_{ij})^\alpha \log(\hat{P}_{ij}) & P_{ij} = 1 \\ (1 - P_{ij})^\beta \hat{P}_{ij}^\alpha \log(1 - \hat{P}_{ij}) & P_{ij} \neq 1 \end{cases}, \quad (2)$$

where α and β are adjustable hyperparameters, N_p is the number of rails in the image, and the term $(1 - P_{ij})^\beta$ is used to reduce the penalty around the ground-truth position.

2) *Starting Point Offset Estimation*: The peak of the predicted heatmap gives a coarse position estimate of the starting point accurate to the stride δ of the feature map. In order to localize the starting point more precisely, we append an additional offset estimation branch to predict an offset map $\hat{O} \in \mathbb{R}^{H_4 \times W_4 \times 2}$. The predicted offset map has two main functions. On the one hand, it eliminates the quantization error introduced during the downsampling process, in which we map

the starting point p to the downsampled position \tilde{p} ; on the other hand, it can correct the starting point position when the starting point predicted by the above heatmap is biased.

In the training stage, we select a square region within distance r around the ground-truth starting point as the valid region and only apply a smooth L1 loss [35] on this valid region to constrain the predicted offset map, as follows:

$$\mathcal{L}_{offset} = \frac{1}{N_p * (2r + 1)^2} \sum_p \sum_{t_y=-r}^r \sum_{t_x=-r}^r SmoothL1Loss(\hat{O}_{\tilde{p}+(t_x, t_y)}, \frac{p}{\delta} - \tilde{p} - (t_x, t_y)), \quad (3)$$

where t_x and t_y are the offsets of the valid position relative to \tilde{p} along the x-axis and y-axis.

3) *Slope Estimation*: A slope estimation branch is added to predict a slope map $\hat{\Theta} \in \mathbb{R}^{H_4 \times W_4}$, which determines the slope of the generated anchor line. A proper slope will make the anchor line fit the rail more closely, making the subsequent rail detection based on the anchor line easier and more precise. Given a rail $L = \{(x_s, y_s), (x_{s+1}, y_{s+1}), \dots, (x_e, y_e)\}$ (here only the valid points of the rail are given for brevity), where $e = s + l - 1$ is the cutoff index of the rail. We compute the average slope of all lines connecting the non-starting point and the starting point on the rail as the ground-truth slope as follows:

$$\theta = \frac{1}{l} \sum_{i=s}^e \arctan2(|y_i - y_s|, |x_i - x_s|), \quad (4)$$

In the training phase, the same valid training region is chosen as the offset estimation and the L1 loss is imposed to constrain the slope prediction, as follows:

$$\mathcal{L}_{slope} = \frac{1}{N_p * (2r + 1)^2} \sum_{k=1}^{N_p} \sum_{t_y=-r}^r \sum_{t_x=-r}^r L1Loss(\hat{\Theta}_{\tilde{p}_k+(t_x, t_y)}, \theta_k), \quad (5)$$

where k is the index of the rail.

4) *Gather Indices and Decode*: In order to decode the corresponding anchor line, we utilize the max pooling and AND operations to find the peaks in the predicted starting point heatmap, and then determine the starting point position and slope based on the peak position, respectively. The max pooling operation naturally eliminates duplicate predictions and it is more efficient than distance-based NMS [11] and IoU-based NMS [21].

Specifically, after the max pooling and AND operations, we can easily obtain the coordinate (\hat{x}, \hat{y}) of each peak in the starting point heatmap. This coordinate is used as a rough starting point position on the one hand, and to associate the corresponding offset and slope on the other. Thus, the final anchor line is determined as $(\delta(\hat{x} + \hat{o}_x), \delta(\hat{y} + \hat{o}_y), \hat{\theta})$, where (\hat{o}_x, \hat{o}_y) is the predicted offset at location (\hat{x}, \hat{y}) in \hat{O} , and $\hat{\theta}$ is the predicted slope at location (\hat{x}, \hat{y}) in $\hat{\Theta}$.

D. Rail Detection Head

In the detection head, the generated anchor line is employed as a reference to accurately localize the final rail.

First, we first extract the RoI feature of the anchor line from the $P3$ feature map. Given the generated anchor line $(x_{start}, y_{start}, \theta)$, we sample N_s points uniformly on it, and then utilize bilinear interpolation to compute the feature of each sampling point. The features of all sampling points are concatenated as RoI features F_{roi} .

Then, to generate the rail proposal, the RoI feature are fed to a fully connected layer, producing N_{pts} horizontal offsets $\Delta X = \{\Delta x_0, \Delta x_1, \dots, \Delta x_{N_{pts}-1}\}$ between the rail and the anchor line, the starting index s and the length l of the rail. In this way, for each fixed $y_i = \frac{H_l}{N_{pts}-1} \times i$, each corresponding predicted x-coordinate \hat{x}_i is calculated as follows:

$$\hat{x}_i = \frac{1}{\tan\theta} \cdot (y_i - y_{start}) + x_{start} + \Delta x_i. \quad (6)$$

The overall loss is defined as follows:

$$\mathcal{L}_{total} = \lambda_{heat}\mathcal{L}_{heat} + \lambda_{offset}\mathcal{L}_{offset} + \lambda_{slope}\mathcal{L}_{slope} + \lambda_{sl}\mathcal{L}_{sl} + \lambda_{LIoU}\mathcal{L}_{LIoU} \quad (7)$$

where \mathcal{L}_{sl} is the smooth L1 loss to supervise the prediction of starting index s and length l . \mathcal{L}_{LIoU} is the Line IoU loss [21], which is calculated based on the predicted rail and the ground-truth rail, and it is used to constrain the offsets regression ΔX . λ_{heat} , λ_{offset} , λ_{slope} , λ_{sl} and λ_{LIoU} are the weight coefficients corresponding to the losses, respectively.

IV. EXPERIMENTS

In order to fully validate the effectiveness of our DALNet, we conduct experiments on our self-built DL-Rail dataset. Tusimple and LLAMAS datasets respectively. Considering that rail detection is a prerequisite for train active obstacle detection, its inference should be fast enough even on edge devices with limited computational resources, so as to allow sufficient time for the obstacle detection algorithms. Therefore, we only select some rapid lane detection models for comparison, which can reason over 200 FPS on our gpu device, promising to be fast enough to run on embedded platforms.

A. Datasets and Evaluation Metric

1) *DL-Rail*: In this paper, we present a challenging urban rail detection dataset. In order to collect the data, we mount cameras at the front of a tram on line 202 in Dalian, Liaoning Province, China, and record videos of forward scenes during the actual train operation, where the video resolution is 1920×1080 . We carefully handpicked 50 videos covering challenging scenarios such as poor lighting and inclement weather. In order to prevent duplication or similarity of scenes in adjacent frames, each video is sampled at 2-second intervals and eventually 7000 images are collected to form the dataset. The dataset is divided into training and test set in the ratio of 8:2. In addition, the test set is further divided according to the scenario categories, which facilitates the evaluation of the model's ability to cope with various types of challenging scenarios, where the scenario categories include normal, nighty, rainy and so on. The examples corresponding to these scenarios are given in Fig. 4.

Compared with other rail detection datasets [3], [4], our dataset is more challenging. On the one hand, many images in

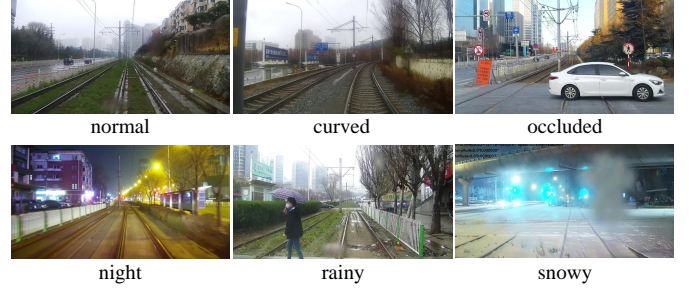


Fig. 4. Dataset examples for different scenarios in our DL-Rail dataset.

our dataset are captured in mixed right-of-way scenarios where rails are often occluded by oncoming vehicles and pedestrians, and on the other hand, many images are recorded under poor lighting and weather conditions where rails are unclear and difficult to recognize and localize.

We use the LabelMe tool to manually annotate the ego rails and each rail is represented by a line strip. When annotating the rails, the history images and contextual information are combined to accurately label the rails if they are occluded or unclear, because the detection of rails in these scenarios is also very important. We hope the users of this dataset can design a model that can utilize global contextual or temporal information to reason about the location of invisible rails as humans do, instead of just giving up on the detection in such scenarios.

The F1-measure is adopted as the metric and it is based on the Intersection-over-union (IoU) between the predicted and ground truth rails. To calculate the IoU, we connect both the predicted and ground truth rail points with width 30 to generate the corresponding mask, and then calculate the IoU between the predicted mask and the ground truth mask. Given an IoU threshold, the prediction is considered as true positive when the IoU of the predicted rail is greater than this threshold. With this condition, we separately statistic the number of true positive (TP), false positive (FP) and false negative (FN) and calculate the F1-measure as follows:

$$F1 = \frac{Precision * Recall}{Precision + Recall}, \quad (8)$$

$$Precision = \frac{TP}{TP + FP}, \quad (9)$$

$$Recall = \frac{TP}{TP + FN}. \quad (10)$$

In this paper, we report the F1@50 and F1@75 metrics for IoU thresholds of 0.5 and 0.75, respectively. In addition, to better compare the performance of the models, we also report a more comprehensive metric mF1 as follows:

$$mF1 = (F1@50 + F1@55 + \dots + F1@95)/10. \quad (11)$$

2) *Tusimple*: Tusimple [30] is a lane detection dataset for real highway scenarios. It contains 3626 training images, 358 validation images and 2782 test images, and all images have 1280×720 pixels. The main evaluation metrics for this dataset

TABLE I
PERFORMANCE ON DL-RAIL

Method	Backbone	mF1	F1@50	F1@75	FPS	GFlops	Normal	Curved	Occluded	Night	Rainy	Snowy
Curve-based												
BézierLaneNet [28]	ResNet18	42.81	85.13	38.62	244	7.55	85.03	80.00	83.33	86.51	85.35	85.24
Keypoint-based												
GANet [13]	ResNet18	57.64	95.68	62.01	208	21.27	99.00	88.00	86.67	93.17	91.22	91.07
Anchor-based												
CondLaneNet [12]	ResNet18	52.37	95.10	53.10	210	10.16	97.73	90.11	86.67	93.05	91.44	91.24
UFLD [10]	ResNet18	53.50	93.67	57.74	398	8.39	95.28	86.24	85.00	92.73	91.29	90.65
UFLD [10]	ResNet34	53.76	94.78	57.15	233	16.9	96.64	89.65	85.00	93.53	91.32	90.77
LaneATT(with FPN) [11]	ResNet18	55.57	93.82	58.97	250	12.46	96.52	85.71	83.33	92.47	91.37	90.83
DALNet (Ours)	ResNet18	59.79	96.43	65.48	212	9.75	99.04	92.24	88.33	94.33	93.92	92.11

are false discovery rate (FDR), false negative rate (FNR) and accuracy, defined as follows:

$$FDR = \frac{FP}{TP + FP}, \quad (12)$$

$$FNR = \frac{FN}{TP + FN}, \quad (13)$$

$$Accuracy = \frac{\sum_{clip} C_{clip}}{\sum_{clip} S_{clip}}, \quad (14)$$

where C_{clip} is the number of correctly predicted lane points and S_{clip} is the number of all ground truth points in the image. For a predicted lane point, it is considered correct only if it lies within 20 pixels of a ground truth point. For a predicted lane, it is considered a true positive when its corresponding prediction accuracy is greater than 85%.

3) *LLAMAS*: LLAMAS [31] is a large-scale lane detection dataset containing over 100,000 images of size 1276×717 , of which 58,269 images are used for training, 20,844 images for validation and 20,929 images for testing. Unlike other datasets, the lane annotations for the LLAMAS dataset are generated automatically with the help of high definition maps. Since the annotations of the test set are not public, the inference results are uploaded to the LLAMAS benchmark’s website for evaluation. The evaluation results include precision, recall and F1-measure.

B. Implementation Details

All the input images are cropped and resized to 800×320 . In order to enhance the generalization, the random horizontal flipping and random affine transformations (rotation, translation, scaling) are adopted as data augmentations. We set the number of sampled points as $N_s = 36$ and $N_{pts} = 72$, and the loss weights are set as $\lambda_{heat} = 1.0$, $\lambda_{offset} = 1.0$, $\lambda_{slope} = 3.0$, $\lambda_{sl} = 0.3$ and $\lambda_{LoU} = 6.0$. For optimization, we use the AdamW optimizer with weight decay of 0.01. The learning rate is initialized with 1.0×10^{-4} , and decayed with a cosine annealing strategy. We train 70 epochs for DL-Rail, 70 epochs for Tusimple, and 20 epochs for LLAMAS. All experiments are performed on 4 Nvidia 3090 GPUS, with a batchsize of 8 per GPU.

C. Results

1) *Results on DL-Rail*: As shown in Tab. I, we compare the performance on the DL-Rail test set with various fast lane detection methods, where the segmentation-based methods are generally slow and therefore not included in the comparison. The results show that our proposed DALNet achieves state-of-the-art results on F1@50, F1@75 and mF1 metrics, demonstrating that DALNet has strong capability for rail detection. In comparison with the curve-based method, DALNet outperforms BézierLaneNet [28] by 16.98 and 11.3 on mF1 and F1@50. Meanwhile, the poor performance of BézierLaneNet [28] indicates the high freedom of rails makes the prediction of control points difficult. GANet [13], as a keypoint-based method, also shows good performance on the rail detection task. In comparison with it, DALNet outperforms it by 2.15 and 0.75 on mF1 and F1@50 with slightly faster inference. CondLaneNet [12] and UFLD [10] are two row-anchor based methods, and DALNet outperforms them on F1@50 by 1.33 and 1.65, respectively. However, UFLD has the fastest inference speed among these methods. In comparison with the line anchor-based method LaneATT [11], DALNet significantly surpasses it by 4.22 and 2.61 on mF1 and F1@50, achieving a better trade-off between speed and localization accuracy.

TABLE II
PERFORMANCE ON TUSIMPLE

Method	Backbone	Acc (%)	FDR (%)	FNR (%)
Curve-based				
BézierLaneNet [28]	ResNet18	95.41	5.30	4.60
Keypoint-based				
GANet [13]	ResNet18	95.95	1.97	2.62
Anchor-based				
UFLD [10]	ResNet18	95.82	19.05	3.92
UFLD [10]	ResNet34	95.86	18.91	3.75
LaneATT [11]	ResNet18	95.57	3.56	3.01
LaneATT [11]	ResNet34	95.63	3.53	2.92
CondLaneNet [12]	ResNet18	95.48	2.18	3.80
DALNet (Ours)	ResNet18	96.68	2.47	2.50

2) *Results on Tusimple*: The results on the Tusimple test set are shown in Tab. II. In comparison with other fast lane detection models, DALNet achieves the best performance on both accuracy and FNR metrics. Specifically, compared to the fastest model UFLD [10], DALNet has a significantly lower

FDR as well as higher localization accuracy. Furthermore, The ResNet18 version of our method outperforms LaneATT [11] (ResNet34) by 1.05 on accuracy, which is already a significant improvement for the Tusimple dataset. These comparison results show that our DALNet also has great potential for lane detection tasks.

TABLE III
PERFORMANCE ON LLAMAS

Method	Backbone	F1 (%)	Precision (%)	Recall (%)
Curve-based				
BézierLaneNet [28]	ResNet18	94.91	95.71	94.13
Anchor-based				
LaneATT [11]	ResNet18	93.46	96.92	90.24
LaneATT [11]	ResNet34	93.74	96.79	90.88
DALNet (Ours)	ResNet18	96.12	96.83	95.42

3) *Results on LLAMAS*: The results on LLAMAS benchmark are shown in Tab. III. Since this benchmark is relatively new, some methods have not submitted their evaluation results. Therefore, only BézierLaneNet [28] and LaneATT [11] methods are incorporated into the comparison. The results show that our DALNet achieves the best performance on F1 and recall metrics, surpassing BézierLaneNet [28] and LaneATT [11] (ResNet34) on F1 by 1.21 and 2.38, respectively, which is significant improvement. These evaluations results are also available on the official benchmark’s website ¹.

D. Ablation Study

To analyze the effectiveness of each composition in our proposed DALNet, the ablation experiments are conducted on our DL-Rail dataset. For our baseline model, we remove the dynamic anchor line generator and directly use fixed anchor lines as references following [11], [20]. To better evaluate our dynamic anchor line mechanism, we further divide it into dynamic anchor line generator (DALG) and dynamic anchor line reference (DALR), where DALG is responsible for the dynamic anchor line prediction, and DALR means that the generated dynamic anchor line is used as a reference for rail localization in the detection head. Tab. IV summarizes the ablation results on our DALG, DALR and pyramidal pooling modules (PPM).

TABLE IV
EFFECTS OF EACH COMPONENT IN OUR METHOD

Baseline	DALG	DALR	PPM	F1@50	F1@75	mF1
✓				94.68	62.81	57.91
✓	✓			94.59	61.35	57.43
✓	✓	✓		96.01	64.09	59.37
✓	✓	✓	✓	96.43	65.48	59.79

1) *Effect of dynamic anchor line generator*: As shown in the second row of Tab. IV, the DALG module is added to the baseline model and is only employed as an auxiliary branch to predict the starting point and slope of the anchor line. However, the results on F1@50, F1@75 and mF1 are consistently decreased compared to baseline. This indicates

that the starting point and slope prediction tasks negatively affect the learning of the rail proposal prediction task, which is widely known as “negative transfer”.

2) *Effect of dynamic anchor line reference*: As shown in the third row of Tab. IV, the DALG and DALR are combined to form a complete dynamic anchor line mechanism, where the anchor line generated by the DALG module is used as a reference. Comparing the results in the second and third rows, we can see that the introduction of DALR improves F1@50, F1@75 and mF1 by 1.42, 2.74 and 1.94, respectively, which indicates that the dynamic anchor line reference can effectively improve the localization performance and it is the key to the whole mechanism. However, it is worth noting that DALG is a prerequisite for DALR, even though its use alone has negative effects.

3) *Effect of pyramid pooling module*: To further enlarge the receptive field, the PPM is inserted between the ResNet backbone and FPN neck. It aggregates contexts with different scales through pyramid pooling. Comparing the third and fourth rows of Tab. IV, the introduction of PPM improves the mF1 and F1@50 metrics by 0.42, indicating that the aggregation of global context can further improve the performance of rail localization. Furthermore, we compare different ways of global context aggregation in Tab. V. The results show that they have relatively similar performance, but PPM achieves the highest mF1 performance and has significantly lower latency than others.

4) *Effect of square supervision region*: For the training of the offset map and slope map predictions, we only supervise the square region of side length $2r + 1$ centered on the ground-truth rail starting point. To verify the effectiveness of this square supervised region, we compare it to the commonly adopted supervised method [38] in which the training is only for keypoint locations. It is worth noting that the latter method is equivalent to ours when r equals 0. As shown in Tab. VI, the best performance can be achieved by setting r to 2, and we improve the F1@50 metric by 0.51 compared to the latter method. This may be attributed to the fact that appropriately enlarging the supervision region can mitigate or even eliminate the detrimental effects of starting point prediction bias.

TABLE V
ABLATION STUDIES OF DIFFERENT CONTEXT AGGREGATION WAYS

Aggregation Ways	F1@50	mF1	Latency (ms)
Self attention [39]	96.47	59.68	1.13
Efficient attention [40]	96.38	59.61	1.03
Strip pooling [41]	96.42	59.59	1.01
PPM	96.43	59.79	0.52

TABLE VI
ABLATION STUDIES OF DIFFERENT SIZE OF SUPERVISION REGION

Supervision region	F1@50	mF1
$r = 0$	95.92	59.41
$r = 1$	96.17	59.55
$r = 2$	96.43	59.79
$r = 3$	96.13	59.57

¹https://unsupervised-llamas.com/llamas/benchmark_splines

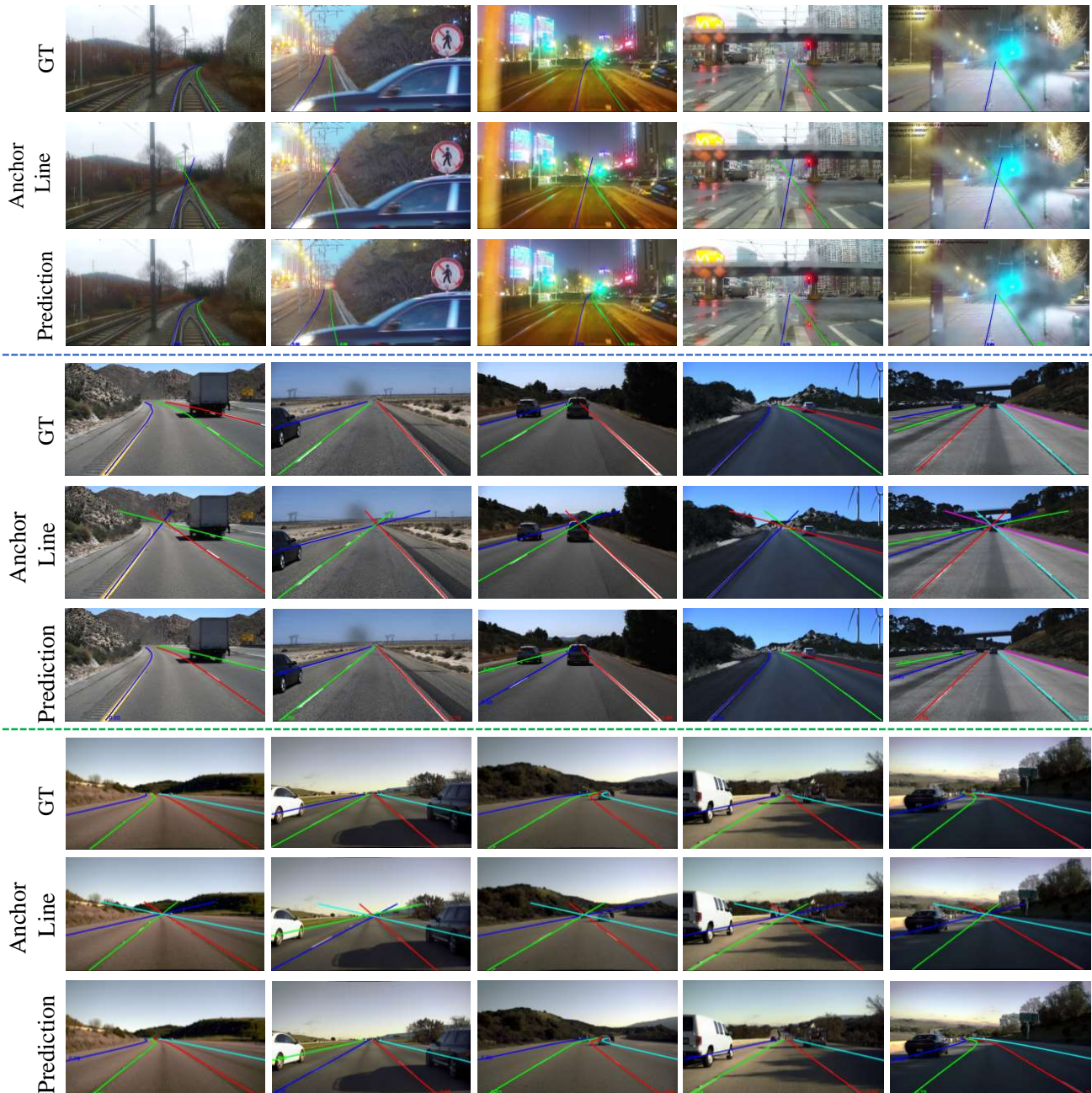


Fig. 5. Qualitative results on DL-Rail(the first row), Tusimple(the middle row) and LLAMAS(the last row) datasets. Different rail or lane instances are drawn in different colors.

E. Qualitative Results

The qualitative results is showed in Fig. 5. Our DALNet can generate a fitted anchor line for each rail or lane instance, even if it is occluded. And it achieves good rail or lane detection performance under different conditions.

V. CONCLUSION

In this paper, we propose a rail detection model DALNet based on dynamic anchor line along with DL-Rail, a scene-diverse urban rail detection dataset. In order to solve the problem that the predefined anchor lines are image agnostic, we introduce a dynamic anchor line generator to generate a

fitted anchor line for each rail instance. We experimentally demonstrate that this dynamically constructed anchor line can be used as a better position reference for rail detection, and can significantly improve the performance of rail detection. In comparison with many fast lane detection methods, Our DALNet achieves state-of-the-art performance on the DL-Rail, Tusimple, and LLAMAS datasets, while still maintaining high efficiency.

REFERENCES

- [1] L. Guan, L. Jia, Z. Xie, and C. Yin, "A lightweight framework for obstacle detection in the railway image based on fast region proposal

- and improved yolo-tiny network,” *IEEE Trans. Instrum. Meas.*, vol. 71, pp. 1–16, 2022.
- [2] T. Ye, J. Zhang, Z. Zhao, and F. Zhou, “Foreign body detection in rail transit based on a multi-mode feature-enhanced convolutional neural network,” *IEEE Trans. Intell. Transp. Syst.*, vol. 23, no. 10, pp. 18 051–18 063, 2022.
- [3] Y. Wang, L. Wang, Y. H. Hu, and J. Qiu, “Railnet: A segmentation network for railroad detection,” *IEEE Access*, vol. 7, pp. 143 772–143 779, 2019.
- [4] X. Li and X. Peng, “Rail detection: An efficient row-based network and a new benchmark,” in *ACM Int. Conf. Multimedia*, 2022, pp. 6455–6463.
- [5] B. T. Nassu and M. Ukai, “A vision-based approach for rail extraction and its application in a camera pan-tilt control system,” *IEEE Trans. Intell. Transp. Syst.*, vol. 13, no. 4, pp. 1763–1771, 2012.
- [6] Z. Qi, Y. Tian, and Y. Shi, “Efficient railway tracks detection and turnouts recognition method using hog features,” *Neural Comput. Appl.*, vol. 23, pp. 245–254, 2013.
- [7] M. H. Zwemer, D. W. van de Wouw, E. G. Jaspers, S. Zinger, *et al.*, “A vision-based approach for tramway rail extraction,” in *Int. Soc. for Opt. Eng.*, vol. 9407. SPIE, 2015, pp. 227–239.
- [8] Y.-S. Zheng, Y.-W. Jin, and Y. Dong, “Rail detection based on lsd and the least square curve fitting,” *Int. J. Automat. Comput.*, vol. 18, no. 1, pp. 85–95, 2021.
- [9] W. Zhangyu, Y. Guizhen, W. Xinkai, L. Haoran, and L. Da, “A camera and lidar data fusion method for railway object detection,” *IEEE Sens. J.*, vol. 21, no. 12, pp. 13 442–13 454, 2021.
- [10] Z. Qin, H. Wang, and X. Li, “Ultra fast structure-aware deep lane detection,” in *Eur. Conf. Comput. Vis.* Springer, 2020, pp. 276–291.
- [11] L. Tabelini, R. Berriel, T. M. Paixão, C. Badue, A. F. De Souza, and T. Oliveira-Santos, “Keep your eyes on the lane: Real-time attention-guided lane detection,” in *IEEE Conf. Comput. Vis. Pattern Recog.*, June 2021, pp. 294–302.
- [12] L. Liu, X. Chen, S. Zhu, and P. Tan, “Conclanenet: A top-to-down lane detection framework based on conditional convolution,” in *Int. Conf. Comput. Vis.*, 2021, pp. 3753–3762.
- [13] J. Wang, Y. Ma, S. Huang, T. Hui, F. Wang, C. Qian, and T. Zhang, “A keypoint-based global association network for lane detection,” in *IEEE Conf. Comput. Vis. Pattern Recog.*, 2022, pp. 1382–1391.
- [14] X. Pan, J. Shi, P. Luo, X. Wang, and X. Tang, “Spatial as deep: Spatial cnn for traffic scene understanding,” in *AAAI*, February 2018.
- [15] T. Zheng, H. Fang, Y. Zhang, W. Tang, Z. Yang, H. Liu, and D. Cai, “Resa: Recurrent feature-shift aggregator for lane detection,” in *AAAI*, vol. 35, no. 4, 2021, pp. 3547–3554.
- [16] G. Pang, B. Zhang, Z. Teng, N. Ma, and J. Fan, “Fast-hbnet: Hybrid branch network for fast lane detection,” *IEEE Trans. Intell. Transp. Syst.*, vol. 23, no. 9, pp. 15 673–15 683, 2022.
- [17] D. Neven, B. D. Brabandere, S. Georgoulis, M. Proesmans, and L. V. Gool, “Towards end-to-end lane detection: an instance segmentation approach,” in *IEEE Intell. Veh. Symp.*, 2018, pp. 286–291.
- [18] Y. Sun, J. Li, X. Xu, and Y. Shi, “Adaptive multi-lane detection based on robust instance segmentation for intelligent vehicles,” *IEEE Trans. Intell. Veh.*, vol. 8, no. 1, pp. 888–899, 2023.
- [19] Z. Qin, P. Zhang, and X. Li, “Ultra fast deep lane detection with hybrid anchor driven ordinal classification,” *IEEE Trans. Pattern Anal. Mach. Intell.*, pp. 1–14, 2022.
- [20] X. Li, J. Li, X. Hu, and J. Yang, “Line-cnn: End-to-end traffic line detection with line proposal unit,” *IEEE Transactions on Intelligent Transportation Systems*, vol. 21, no. 1, pp. 248–258, 2019.
- [21] T. Zheng, Y. Huang, Y. Liu, W. Tang, Z. Yang, D. Cai, and X. He, “Clrnet: Cross layer refinement network for lane detection,” in *IEEE Conf. Comput. Vis. Pattern Recog.*, June 2022, pp. 898–907.
- [22] Y. Ko, Y. Lee, S. Azam, F. Munir, M. Jeon, and W. Pedrycz, “Key points estimation and point instance segmentation approach for lane detection,” *IEEE Trans. Intell. Transp. Syst.*, 2021.
- [23] Z. Qu, H. Jin, Y. Zhou, Z. Yang, and W. Zhang, “Focus on local: Detecting lane marker from bottom up via key point,” in *IEEE Conf. Comput. Vis. Pattern Recog.*, 2021, pp. 14 117–14 125.
- [24] Z. Yao, X. Wu, P. Wang, and C. Ding, “Devnet: Deviation aware network for lane detection,” *IEEE Trans. Intell. Transp. Syst.*, vol. 23, no. 10, pp. 17 584–17 593, 2022.
- [25] L. Tabelini, R. Berriel, T. M. Paixão, C. Badue, A. F. De Souza, and T. Oliveira-Santos, “Polylanenet: Lane estimation via deep polynomial regression,” in *Int. Conf. Pattern Recog.*, 2021, pp. 6150–6156.
- [26] R. Liu, Z. Yuan, T. Liu, and Z. Xiong, “End-to-end lane shape prediction with transformers,” in *WACV*, 2021, pp. 3693–3701.
- [27] B. Wang, Z. Wang, and Y. Zhang, “Polynomial regression network for variable-number lane detection,” in *Eur. Conf. Comput. Vis.* Springer, 2020, pp. 719–734.
- [28] Z. Feng, S. Guo, X. Tan, K. Xu, M. Wang, and L. Ma, “Rethinking efficient lane detection via curve modeling,” in *IEEE Conf. Comput. Vis. Pattern Recog.*, 2022, pp. 17 041–17 049.
- [29] H. Chen, M. Wang, and Y. Liu, “Bsnet: Lane detection via draw b-spline curves nearby,” *arXiv preprint arXiv:2301.06910*, 2023.
- [30] TuSimple, “Tusimple benchmark.” <https://github.com/TuSimple/tusimple-benchmark/>, Accessed September, 2020.
- [31] K. Behrendt and R. Soussan, “Unsupervised labeled lane marker dataset generation using maps,” in *Int. Conf. Comput. Vis.*, vol. 1, 2019, p. 7.
- [32] D. Comaniciu and P. Meer, “Mean shift: a robust approach toward feature space analysis,” *IEEE Trans. Pattern Anal. Mach. Intell.*, vol. 24, no. 5, pp. 603–619, 2002.
- [33] A. Newell, K. Yang, and J. Deng, “Stacked hourglass networks for human pose estimation,” in *Eur. Conf. Comput. Vis.*, 2016.
- [34] H. Zhao, J. Shi, X. Qi, X. Wang, and J. Jia, “Pyramid scene parsing network,” in *Proceedings of the IEEE conference on computer vision and pattern recognition*, 2017, pp. 2881–2890.
- [35] S. Ren, K. He, R. Girshick, and J. Sun, “Faster r-cnn: Towards real-time object detection with region proposal networks,” *IEEE Trans. Pattern Anal. Mach. Intell.*, vol. 39, no. 6, pp. 1137–1149, 2017.
- [36] T.-Y. Lin, P. Goyal, R. Girshick, K. He, and P. Dollár, “Focal loss for dense object detection,” *IEEE Trans. Pattern Anal. Mach. Intell.*, vol. 42, no. 2, pp. 318–327, 2020.
- [37] T.-Y. Lin, P. Dollár, R. Girshick, K. He, B. Hariharan, and S. Belongie, “Feature pyramid networks for object detection,” in *Proceedings of the IEEE conference on computer vision and pattern recognition*, 2017, pp. 2117–2125.
- [38] H. Law and J. Deng, “Cornernet: Detecting objects as paired keypoints,” in *Eur. Conf. Comput. Vis.*, 2018, pp. 734–750.
- [39] A. Vaswani, N. Shazeer, N. Parmar, J. Uszkoreit, L. Jones, A. N. Gomez, L. Kaiser, and I. Polosukhin, “Attention is all you need,” in *Adv. Neural Inform. Process. Syst.*, 2017, p. 6000–6010.
- [40] S. Zhuoran, Z. Mingyuan, Z. Haiyu, Y. Shuai, and L. Hongsheng, “Efficient attention: Attention with linear complexities,” in *WACV*, 2021, pp. 3530–3538.
- [41] Q. Hou, L. Zhang, M.-M. Cheng, and J. Feng, “Strip pooling: Rethinking spatial pooling for scene parsing,” in *IEEE Conf. Comput. Vis. Pattern Recog.*, 2020, pp. 4002–4011.